A Comparison of Sigma Phase Formation in Solubilized Hyper Duplex Stainless Steel and Super Duplex Stainless Steel Filler Metals



ANDRES ACUNA (D), KAUE CORREA RIFFEL (D), and ANTONIO RAMIREZ (D)

This study focuses on the kinetic analysis of sigma phase formation in filler metal wires on Super Duplex Stainless Steel (SDSS) and Hyper Duplex Stainless Steel (HDSS). Precipitation data reveal that in the solubilized microstructure, sigma phase kinetics are more prominent in SDSS. This increased susceptibility is attributed to the greater number of nucleation sites, which is facilitated by the larger interface area/volume and the higher chromium content in the ferrite. The difference in interface area/volume is significantly more influential in determining kinetics than the composition difference, with nucleation sites playing a central role. The sigma phase transformation in both materials was modeled using the JMAK kinetic law. The JMAK plots exhibit a transition in kinetic mechanisms, evolving from discontinuous precipitation to diffusion-controlled growth. In SDSS, the JMAK values indicate "grain boundary nucleation after saturation," followed by "thickening of large plates." In contrast, HDSS values point to "grain edge nucleation after saturation," followed by "thickening of large needles." The higher kinetics in SDSS are characterized by a smaller nucleation activation energy of 56.4 kJ/mol, in contrast to HDSS's 490.0 kJ/mol. CALPHAD-based data support the JMAK results, aligning with the maximum kinetics temperature of SDSS (875 °C to 925 °C) and HDSS (900 °C to 925 °C). Therefore, the JMAK sigma phase kinetics effectively describe the experimental data and its dual kinetics behavior, even though CALPHAD-based TTT calculations often overestimate sigma formation.

https://doi.org/10.1007/s11661-024-07442-4 © The Author(s) 2024

I. INTRODUCTION

Duplex Stainless Steels (DSS) find extensive industrial use due to their exceptional attributes encompassing corrosion resistance, hardness, toughness, and yield strength. Achieving a balanced microstructure approximating 50 pct ferrite and 50 pct austenite is pivotal to their processing. The localized corrosion resistance hinges on the material's composition and is typically gauged using the pitting resistance equivalent number (PREn). The PREn takes into account key elements such as chromium (Cr), molybdenum (Mo), and nitrogen (N) in its empirical calculation. The DSS materials are classified

based on PREn, using its most common formulation: PREn = pct Cr + 3.3*(pct Mo + 0.5* pct W) + 16* pct N in weight.^[1,2]

Recent history has favored Super Duplex Stainless Steel for its enhanced corrosion performance within a PREn range of 40 to 45. The advent of Hyper Duplex Stainless Steel (HDSS) has pushed this limit even further, surpassing a PREn of 48. However, the heightened alloying for improved corrosion properties brings forth challenges in microstructure stability. Elevated temperatures between 600 °C and 1100 °C could trigger intermetallic precipitation, including the formation of sigma phase and chi phase. Among these, sigma phase is the prominent precipitate in highly alloyed DSS. [3] It prefers to nucleate at the interfaces of austenite and ferrite as well as grain edges. Once formed, these phases grow within the ferrite phase, depleting Cr and Mo, subsequently leading to reduced corrosion resistance^[4,5] and compromised mechanical properties.[5-7]

While previous studies have addressed sigma phase formation and its implications on austenitic stainless steels, [8,9] and ferritic stainless steels, [10,11] duplex stainless steels, [12–17] and SDSS, [18–27] there remains a scarcity of research concerning HDSS. [28–32] Moreover, the predominant focus has been on intermetallic formation in DSS, specifically exploring the effects on base metals

ANDRES ACUNA is with the Consumable R&D, Lincoln Electric Cleveland, 22801 Saint Clair Avenue, Euclid, OH 44117. KAUE CORREA RIFFEL and ANTONIO RAMIREZ are with the Materials Science and Engineering/Welding Engineering Program, The Ohio State University, 1248 Arthur E. Adams Drive, Columbus, OH 43221. Contact e-mail: ramirez.49@osu.edu

Manuscript submitted February 11, 2024; accepted May 13, 2024. Article published online June 17, 2024

Table I. Measured Chemical Composition in Weight Percent for the Rod Samples Used in Physical Simulation and the CALPHAD-based Kinetic Model

Material	Fe	С	Cr	Ni	Mo	N	Co	Mn	PREn
HDSS 27.7.5.L	Bal.	0.023	26.05	6.31	4.74	0.4	1.32	0.96	48.0
Standard Error* ± pct	0.101	0.0009	0.026	0.046	0.036	0.018	0.003	0	N/A
SDSS ER2594	Bal.	0.01	25.05	9.25	3.90	0.27	0.05	0.42	42.2
Standard Error* ± pct	0.422	0.0065	0.082	0.234	0.065	0.031	0.031	0.012	N/A

^{*}Standard Error calculated for a 95 pct interval of confidence.

and heat-affected zones. In particular, there has been limited attention directed towards the effects of intermetallics on weld metal, with an even scarcer consideration of sigma phase kinetics in filler metals. Given applications like cladding, welding, and additive manufacturing often involve extensive weld metal, understanding and controlling the sigma phase in these contexts are crucial. In a prior investigation, Acuna and Ramirez^[33] presented a sigma phase kinetics analysis to control sigma phase in HDSS solubilized wire. Later, Acuna *et al.*^[34] used the developed kinetics model to produce sigma phase-free HDSS layers cladding multiple tubesheet mockups with excellent toughness and corrosion performance.

Building on this foundation, the current study extends the previously developed sigma phase kinetics analysis to the widely used SDSS ER 2594, [35] evaluating kinetics in the solubilized microstructure. [36] This analysis is juxtaposed with the more alloyed HDSS wire, also in its solubilized state. By employing analytical calculations grounded in both experimental and CALPHAD-based data, this research yields an enhanced understanding of the materials' vulnerability to sigma phase formation.

II. MATERIALS AND METHODS

Two specimens of filler metal materials were extracted from pre-drawn rods characterized by an outer diameter of 5.6 mm. The chemical composition analysis of these materials was conducted using Optical Emission Spectroscopy (OES), and the nitrogen content was additionally confirmed using a combustion spectrometer Leco TC600 and is summarized in Table I. The rods underwent a solubilization process during production. Examination through optical and scanning electron microscopy revealed a minimal presence of sigma phase in the solubilized state for the SDSS material, whereas no sigma phase was observed in the HDSS material.

A. Precipitation Heat Treatment

The experimental design employed in this study aimed to generate a precipitation map by utilizing a Gleeble 3800 physical simulator. This apparatus subjected filler metal rods to a rapid heating rate of 100 °C/s until a predetermined isothermal aging temperature was attained. Subsequently, this temperature was maintained for a specified aging duration, followed by a cooling process with a minimum rate of 37 °C/s. The

details of the precipitation procedure are presented elsewhere in the literature^[32,33] and are described in the supplementary material, Figure S1.

For each sample, microstructural characterization was performed to determine the corresponding volumetric fraction of intermetallic phases. The measured volumetric fractions, along with the associated time and temperature data, were utilized to construct the time–temperature–transformation (TTT) contour plot map, which represents experimental kinetics. To develop this map, the data points were interpolated using the Kriging^[37] method. The isovolumetric lines depicted in the map represent the interpolated kinetic TTT curves.

B. Microscopic Characterization

Intermetallic volume fractions were quantified using both optical microscopy (Olympus DP2-BSW microscope) and electron microscopy (FEI Apreo LoVac High Resolution). The samples underwent a preparation process that involved grinding from 240 to 1200 grit, followed by polishing with 1 μ m diamond paste and a final polishing step with 0.02 um colloidal silica for three hours. To reveal the microstructure, a dual-step electro etching process using a solution of 40 pct HNO₃ and 60 pct distilled water was performed. The first step involved applying a voltage of 1.3 V for 20 seconds to etch the interphases, while the second step utilized a voltage of 0.9 V for 60-240 seconds to preferentially etch the ferrite, modification from Ramirez et al.[38] This etchant was chosen to highlight the intermetallic properties (appearing white), while allowing for clear contrast between the ferrite (brown/caramel) and austenite (tan/yellow) phases, as shown in Figure 1.

Quantification of phase fractions was achieved through digital image analysis of both the optical microscopy and electron microscopy fields. In this analysis, gray-scale images were subjected to threshold filtering to select and quantify the ferrite, austenite, chi phase, and sigma phase individually. The volume fraction data reported are averaged values obtained from at least five randomly selected fields at 1000x magnification. [32,39] For details on the phase volume measurement methodology, refer to electronic supplementary material, Figure S2, Table S1, and Table S2.

C. JMAK Kinetics Calculations

The formation of sigma phase, with respect to temperature and time, has been elucidated through the utilization of the Johnson–Mehl–Avrami–Kolmogorov (JMAK) kinetic law, [40–42] expressed as follows:

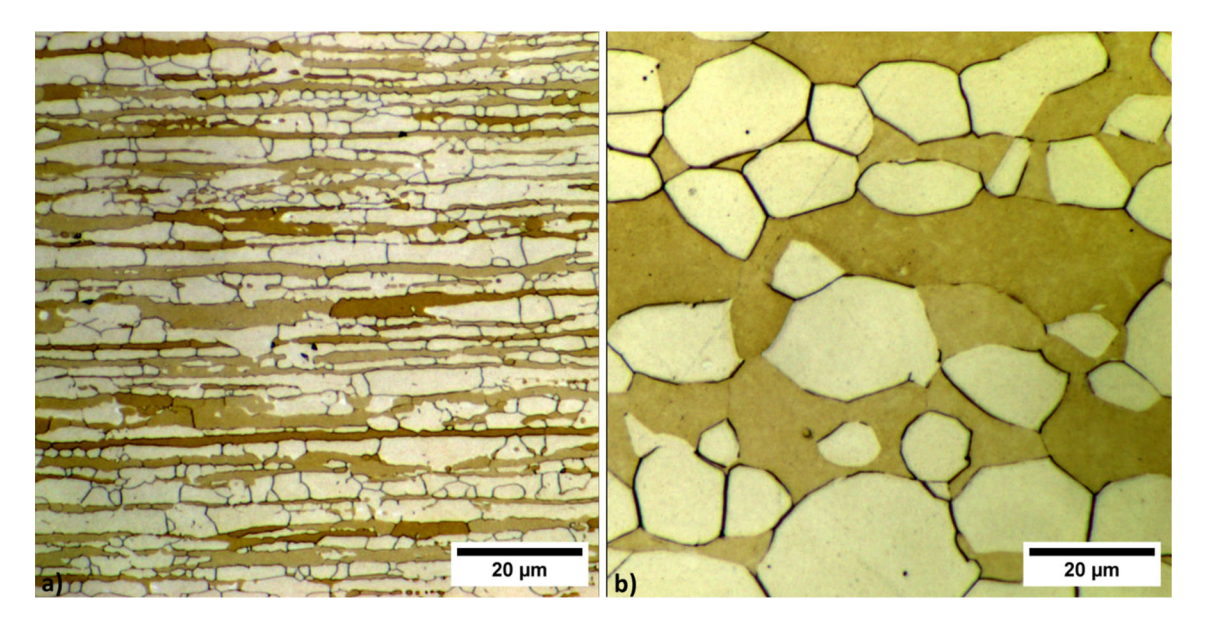


Fig. 1—LOM of the physical simulation specimen initial microstructure (a) SDSS and (b) HDSS. Etchant 40 pct HNO₃ + 60 pct distilled water, revealing austenite as the brighter phase and ferrite as the tan/brown phase.

$$f = 1 - e^{(-kt^n)}$$

where f represents the fraction of transformed sigma phase volume (0 < f < 1), t denotes the transformation time, and n signifies Avrami's exponent, which characterizes the order of solid-state reactions. The variable k is associated with the energy barrier for sigma phase formation and is mathematically described by the Arrhenius equation:

$$k = k_0 e^{\left(-\frac{Q_{\sigma}}{RT}\right)},$$

where k_0 represents the pre-exponential constant, Q_{σ} denotes the activation energy for sigma phase nucleation and growth, T represents the temperature in Kelvin, and R denotes the gas constant.

In this analytical approach, the experimental precipitation data were obtained by measuring at 25 °C intervals within the temperature range of 775 °C to 1000 °C. The JMAK equation was linearized to generate $ln(-ln(1-f)) \times ln(t)$ plots, which provide graphical representations of sigma phase kinetics.

By analyzing these linearized plots, the Avrami's exponent (n) and the time activation factor (k) were determined. The fitted inclination defines the exponent n. This relates directly to the transformation mechanism. Simultaneously, variable k can be calculated via the vertical intercept and is related to the activation energy for the sigma phase formation. $[^{41,43,44}]$

D. CALPHAD-Based Kinetics Modeling

The precipitation kinetics of the sigma phase is modeled within a CALPHAD-based system, utilizing the TCFE11 and MOBFE6 databases. These CALPHAD-based calculations are utilized to construct time-temperature-transformation (TTT) curves. The model incorporates parameters related to nucleation

site distribution and nucleation barriers, including interfacial energy. These parameters are adjusted based on experimental data, as demonstrated by Acuna *et al.*^[32] and Acuna and Ramirez.^[33]

III. RESULTS AND DISCUSSION

A. Material and Microstructure Characterization

Although the materials were drawn to the same rod diameter and had a similar solubilization process, the materials' microstructures exhibited significant differences. Figure 1 compares the microstructures, showing the SDSS (a) with approximately 39.5 ± 0.5 pct ferrite and the HDSS (b) with around 49.5 ± 0.3 pct ferrite. These variations in microstructural distribution, grain size, aspect ratio, and total interface contribute to differences in transformation kinetics. [45]

The materials' solubilized initial conditions are presented in optical micrography. Although the materials were drawn to the same rod diameter and have a similar solution heat treatment, the SDSS microstructure is more refined and elongated grains than the HDSS. Table II presents data from EBSD measurements showing the SDSS grains are one order of magnitude smaller than the HDSS.

The SDSS reduced grain size area, in particular the ferrite is significant because sigma phase formation primarily occurs through ferrite decomposition. Consequently, the diffusion distances within the SDSS are shorter. Moreover, the aspect ratio and phase distribution impact the total interface length, which determines preferential sites for sigma phase nucleation.

Figure 2 presents the segmentation of EBSD data, focusing on ferrite grains. The subsequent analysis calculates the total interface length between austenite and ferrite per unit volume for both the SDSS (a) and HDSS (b). The results, summarized in Table II, indicate

Table II. Solubilized Microstructure SEM EBSD Measurements

	Both	phases	Aus	stenite	Ferrite		
	Average [μ m ²]	Std. Ε.* ± [μm]	Average [μm ²]	Std. Ε.* ± [μm]	Average [μm ²]	Std. E.* \pm [μ m]	
SDSS HDSS			8.79 3.46 80.16 34.15		2.11 64.61	0.66 25.42	
	Interface	e length/volume calcu	lation				
Material	Image Area [µm] ²		In	terfacial length [µm]	Interface area/Volume [μm ⁻¹]		
SDSS HDSS	799.2 4910.1			580.5 953.50	0.726 0.194		

Phase's grain size area and interface area/volume steps calculation: image area, interface length, and interface area/volume. Note: Each calculated interface length/volume was measured on a specific EBSD Map for a standard error calculation more EBSD maps measurements are needed.* Standard Error calculated for a 95 pct interval of confidence.

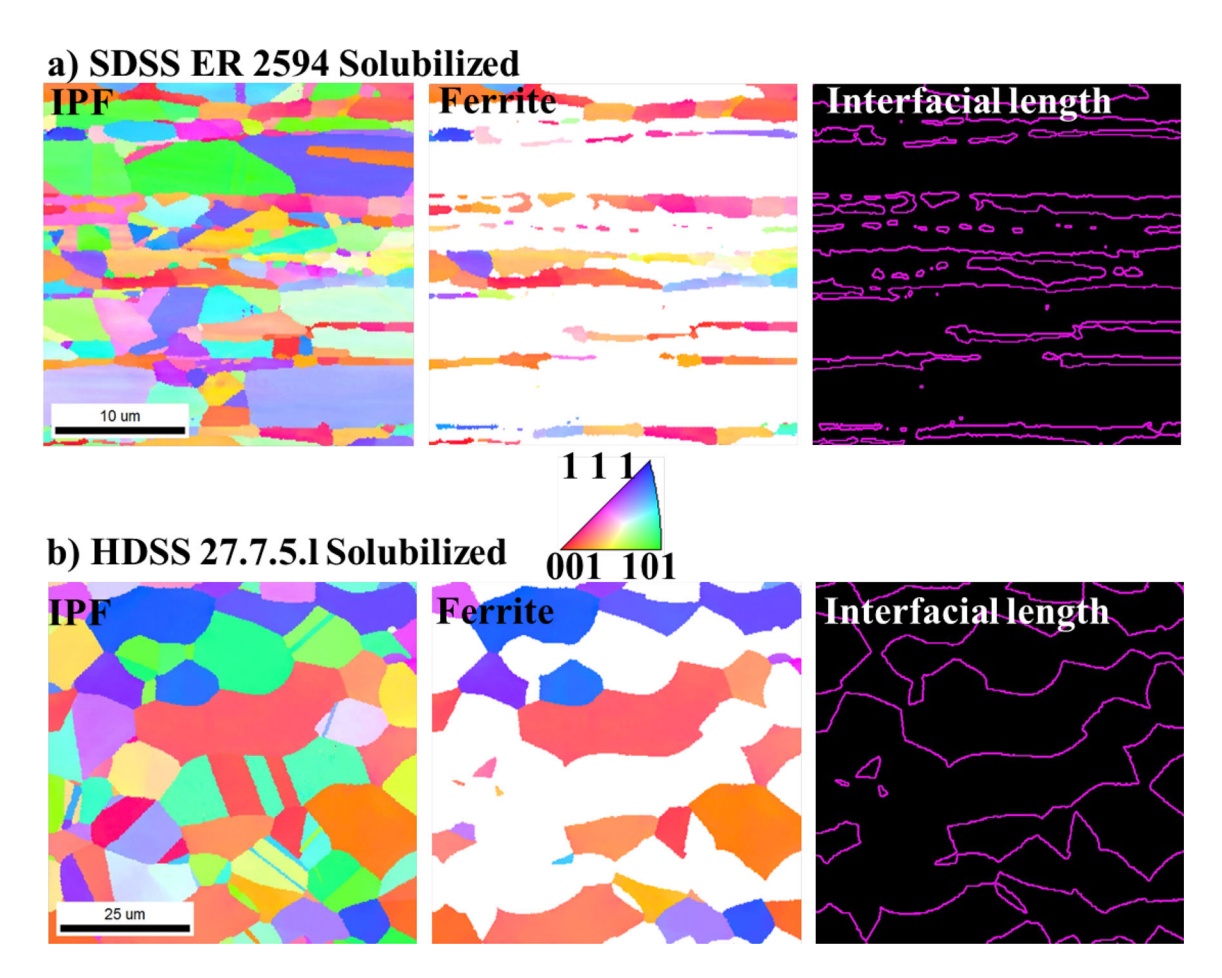


Fig. 2—Solubilized Microstructure SEM EBSD measurements. Inverse pole figure of both phases, IPF ferrite segmentation and ferrite segmented interface length of SDSS wire (a) and HDSS wire (b).

that the SDSS exhibits 374 pct more interfacial length per unit volume compared to the HDSS. This increased interfacial area provides favorable sites for nucleation, thereby influencing the kinetics of phase transformation.

It is important to note that the images in Figure 2 are captured at different magnifications due to the smaller grain size of the SDSS, requiring higher magnification to resolve its microstructure. Both analyses were conducted

using a step size of 0.1 μ m. However, all measurements have been normalized to the image area in Table II, ensuring direct comparability between the samples.

Microstructural analysis indicates that sigma phase nucleation may occur more rapidly in the SDSS due to its higher interface lengths. Furthermore, the reduced ferrite grain area suggests a faster growth rate. However, the exhaustion of ferrite (resulting in a smaller

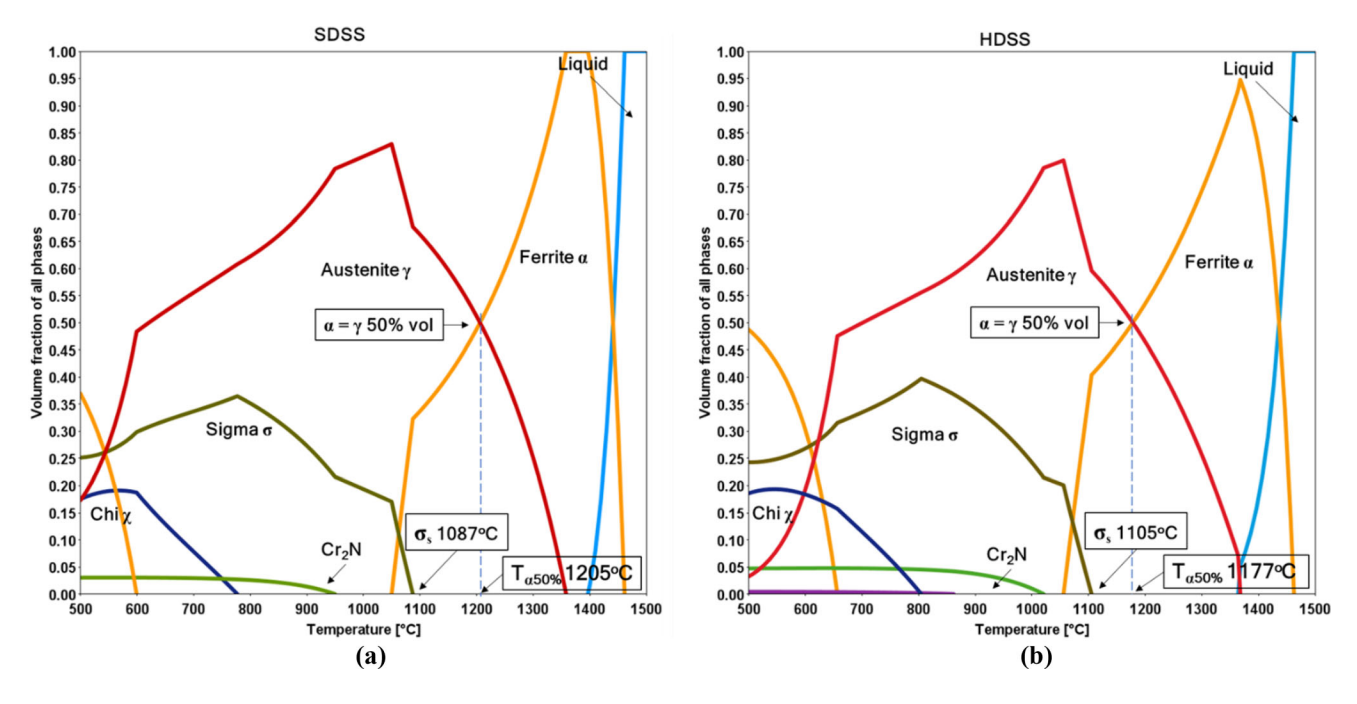


Fig. 3—CALPHAD equilibrium simulation (TCFE11 database), phases volumetric fraction distribution as a function of temperature.

volumetric fraction) could impede growth and prolong the time required to reach the equilibrium volume. In contrast, the microstructure analysis of the HDSS suggests longer nucleation times for the sigma phase and a higher growth rate towards the equilibrium volume.

Figure 3 displays the thermodynamic equilibrium phase volume fraction distribution as a function of temperature for both materials based on CALPHAD calculations (TCFE11 database). The thermodynamic diagrams exhibit similarities due to the comparable chemical composition of the materials. However, the nitrogen content, and its influence on the ferrite matrix phase, is a key distinguishing factor. Zhang *et al.*^[30] have shown the impact of nitrogen on the precipitation behavior of HDSS, highlighting its role in the distribution of chromium (Cr) and molybdenum (Mo). Increasing nitrogen content leads to a smaller difference in Cr and Mo concentrations between the austenite and ferrite phases. Furthermore, higher nitrogen levels have been found to reduce the sigma phase nucleation.

SDSS has a fully ferritic solidification, while HDSS, enriched with austenite stabilizers like Ni and N, promotes austenite formation during solidification. This composition reduces ferrite volume and grain size, increasing austenite content. Table III presents thermodynamic calculations and SEM EDS measurements of the phase's chemical composition at corresponding sigma solvus temperatures (1087 °C for SDSS, 1105 °C for HDSS).

Acuna *et al.*^[34] compared HDSS chemical composition equilibrium calculations varying the nitrogen 0.2, 0.3, and 0.4 pct in weight. In equilibrium, the austenite stabilizing role of nitrogen has critical influence on solidification. Below 0.35 wt pct nitrogen solidification occurs through ferrite and austenite will only form on solid state. Tis solidification path causes ferrite grain growth enriches it

with Cr and Mo. Conversely, the higher N content promotes some austenite volume on solidification, this hinders the ferrite grain size and phase volume. As consequence, it reduces sigma phase volume as there is less ferrite available to transform into sigma phase.

The EDS results indicate higher Cr content in SDSS ferrite compared to HDSS, which is a critical element for sigma phase nucleation and growth. Additionally, SDSS exhibits significant Cr and Mo differences between the phases. In contrast, the higher nitrogen content in HDSS influences the partitioning of Cr and Mo, resulting in similar PREn values for austenite and ferrite. This leads to austenite with higher localized corrosion resistance at the expense of reduced Cr and Mo content in ferrite. [46–48]

Previous studies by Kim *et al.*^[29] measured the chemical composition of phases using EDS in HDSS alloys with varying Mo contents. They found very similar Cr content in both ferrite (26.51 pct) and austenite (25.26 pct). Similarly, Wang *et al.*^[31] measured the phase compositions in the solubilized condition and after multiple aging times, showing only a 1 pct difference in Cr content. These findings align with the measured values presented in Table III.

B. Microstructural Characterization and Kinetics

Quantitative metallography was conducted on samples from the isothermal precipitation experiment, providing data on time, temperature, and sigma phase volume fraction. These data were extrapolated to generate experimental interpolated contour maps for the sigma phase^[32,33] in Figure 4. The CALPHAD-adjusted time–temperature–transformation (TTT) curves corresponding to volumetric fractions of 1, 5, and 10 pct were overlapped on the interpolated experimental precipitation map, indicated by dashed lines.

Table III. Phases' Chemical Composition: EDS Measurements and Thermodynamic Calculations at Sigma Phase Solvus Temperature, 1087 °C and 1105 °C for the SDSS and HDSS, Respectively

EDS measured phase's composition								
Material	Phases	Cr	Mo	Ni	Со	Mn	Fe	PREn
SDSS	Ferrite [wt pct]	27.7	3.8	6.3	2.0	1.6	57.7	N/A
	Std. E. [± pct]	1.0	0.3	0.9	0.0	0.1	0.5	•
	Austenite [wt pct]	24.5	2.8	8.9	2.0	1.5	58.9	N/A
	Std. E. [± pct]	1.0	0.3	0.9	0.0	0.0	0.5	•
HDSS	Ferrite [wt pct]	26.3	3.5	6.1	2.7	2.0	57.6	N/A
	Std. E. [± pct]	0.6	0.5	0.7	0.1	0.0	0.1	,
	Austenite [wt pct]	26.0	3.2	6.4	2.7	2.0	57.7	N/A
	Std. E. [± pct]	0.5	0.4	0.6	0.1	0.0	0.1	,

Thermodynamic phase's composition calculation at Sigma solvus temperature								
Material	Phases	Cr	Mo	Ni	Co	Mn	Fe	PREn
SDSS	Ferrite wt pct	28.4	5.1	6.4	0.044	0.05	59.9	46.0
	Austenite wt pct	23.5	3.3	10.9	0.053	0.34	61.6	39.8
	Sigma wt pct	32	11.8	5.44	0.36	0	50.7	N/A
HDSS	Ferrite wt pct	27	6.23	5	1.2	0.07	60.3	48.8
	Austenite wt pct	25.3	4	7.8	13	0.62	60.8	48.5
	Sigma wt pct	30.2	14.0	4.2	1.0	0	57.7	N/A

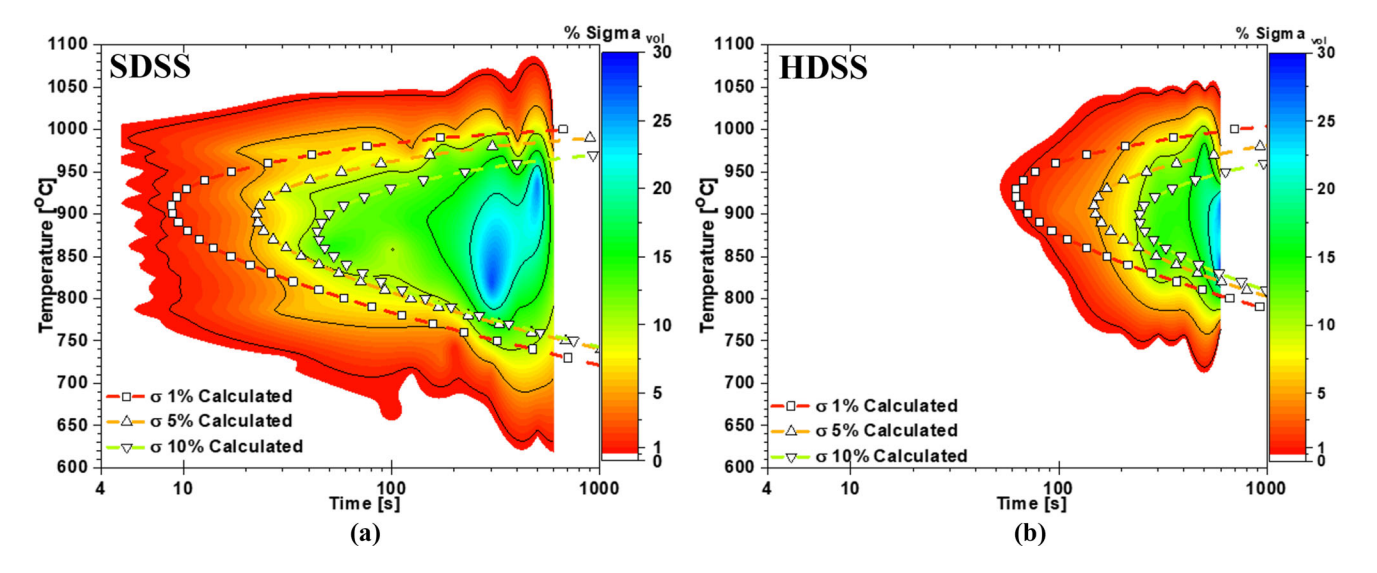


Fig. 4—Sigma phase kinetics TTT maps. Calphad precipitation TTT overlapped on the experimental interpolated contour plot of SDSS (a) and HDSS (b).

Figure 4 presents experimental data illustrating the kinetics of the sigma phase in solubilized conditions for both SDSS and HDSS filler metals. The measurement methodology, complete dataset including the standard error of every measurement is included on the supplementary material. The results indicate higher sigma phase kinetics in the SDSS compared to the HDSS, considering the solubilized filler metal form and chemical compositions employed. Nucleation occurs earlier, and the growth rate is also higher in the SDSS. The precipitation temperature range for the SDSS (650 °C – 1050 °C) is wider than that of the HDSS (750 °C – 1050 °C). Moreover, the SDSS demonstrates a broader temperature range (775 °C – 1000 °C) within

the region of maximum kinetics, whereas the HDSS is limited to the 900 $^{\circ}$ C - 950 $^{\circ}$ C range.

The sigma phase formation kinetics exhibit notable variations between the two materials. In the case of SDSS, a 1 pct volume fraction of sigma phase is achieved within 5.0 s, while reaching 10 pct volume fraction takes 36.5 s. Conversely, HDSS requires 63.3 s for 1 pct volume fraction and 225.0 s for 10 pct volume fraction. Particularly noteworthy is the more rapid transformation rate in SDSS, where the volume fraction transitions from 1 to 10 pct within 35.7 s. In contrast, HDSS necessitates 110.5 s to cover the same sigma phase volume range.

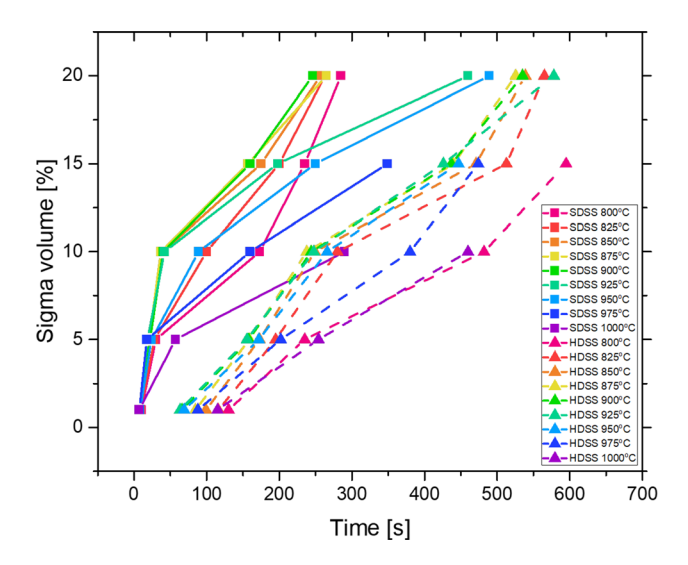


Fig. 5—Isothermal transformation volume fraction as a function of time for multiple temperatures. Square symbols show the SDSS solubilized microstructure, and triangle symbols reproduce the HDSS solubilized microstructure.

The considerable disparity in sigma phase kinetics is unlikely solely attributed to chemical composition. Although HDSS exhibits higher Cr and Mo contents, suggesting potential for enhanced sigma phase kinetics, this might be counterbalanced by its higher N content and increased amount of austenite. A previous study^[35] compared the sigma phase kinetics of the same two materials on the as-welded condition using the same welding parameters. However, the as-welded microstructure presented an equivalent interface length/volume. Therefore, the analysis referred to the chemical composition's role on sigma phase kinetics. It was found that for a sigma phase volume of 1 pct, the kinetics of both materials was equivalent, whereas for volumes of 5 pct and 10 pct, the higher Cr and Mo content on HDSS played a role on a slightly faster growth.

Therefore, the substantial kinetics difference seen in this research, such as on Figure 4 suggest the presence of additional influencing factors on kinetics. The SDSS solubilized wire's 374 pct higher interface length per volume unit is understood as the primary driver for its elevated sigma phase kinetics. The higher interface length per volume unit is translated to a higher nucleation site density, which is attributed to the higher kinetics. For instance, the classical nucleation theory implemented on the CALPHAD-based kinetic model uses the nucleation site density as a direct multiplier on the formed phase volume. [49–51]

Figure 4 contour plots were generated using the Kriging interpolation method, which provides excellent visual representations of the data. However, due to adjustment methods between the experimental data points, the plotted TTT shape exhibits some intrinsic waviness. Nonetheless, the continuous black lines accurately represent the true experimental interpolated TTT curves.

Figure 5 compares the transformation rates of both materials at various volumetric fractions (1 pct, 5 pct,

10 pct, 15 pct, and 20 pct) for sigma phase formation. The continuous lines with square markers represent the SDSS, while the dashed lines with triangle markers represent the HDSS. The plot clearly illustrates that the SDSS exhibits a higher transformation rate for sigma phase precipitation compared to the HDSS.

For both materials, an inflection point in the transformation rate occurs around 5 pct volumetric fraction at lower precipitation temperatures (T < 800 °C). At these temperatures, undercooling promotes nucleation, but diffusion is limited. Equivalently, another inflection point is observed also around 5 pct volumetric fraction at the upper end of the precipitation temperature range (T < 975 °C). Here, low undercooling hinders nucleation, but diffusion is high.

Apart from the extreme ends of the precipitation temperature range, both materials display a significant change in the transformation rate around 10 pct sigma phase formation, indicating a shift in the underlying transformation mechanism. At the temperature range of maximum kinetics, a balance between nucleation and diffusion leads to a rapid transformation rate until a certain volumetric fraction is reached. Subsequently, as nucleation sites become scarce, diffusional growth consumes the available Cr and Mo, leading to a rapid increase in the transformation rate. This transition in kinetic mechanism has been reported in other studies on DSS kinetics, [3,26,52,53] and will be further discussed on Kinetics calculations section, where the JMAK analysis provided quantification of the kinetics change.

In both materials, the CALPHAD-based TTT adjustments show excellent agreement with the experimental data at the time and temperature corresponding to maximum kinetics. However, it should be noted that the CALPHAD model's temperature range is more limited. Consequently, the model fails to accurately capture the transformations occurring at both high and low temperatures, regardless of the material.

Figure 6 displays backscattered electron SEM images showcasing the microstructure evolution of the solubilized filler metals, with SDSS on the left column (a-d) and HDSS on the right column (e-f). In the solubilized condition, SDSS exhibits rapid kinetics, with sigma phase nucleation occurring within 15 seconds at 935 °C, close to the maximum kinetics, 6.27 ± 1.01 pct of sigma phase forms, Figure 6(a). Sigma grains grow along elongated ferritic grains, primarily nucleating at triple corners.

In 175 seconds, 11.24 \pm 1.49 pct sigma phase volume is observed, even at lower temperatures such as 728 °C, Figure 6 (b). Nucleation is facilitated at temperatures below the maximum kinetics due to increased undercooling, but limited diffusion hampers growth. This leads to the formation of colonies of tortuous sigma phase and secondary austenite structures, as reported by Pohl *et al.* ^[54] and Zhang *et al.* ^[28]

At 817 °C, a substantial volume of sigma phase $(27.93 \pm 0.81 \text{ pct})$ is formed, depicting the wide precipitation temperature range in this alloy and condition. Extensive eutectoid decomposition is observed in $\sigma + \gamma 2$ colonies, consuming a significant portion of the available ferrite, Figure 6 (c). A distinct lamellar

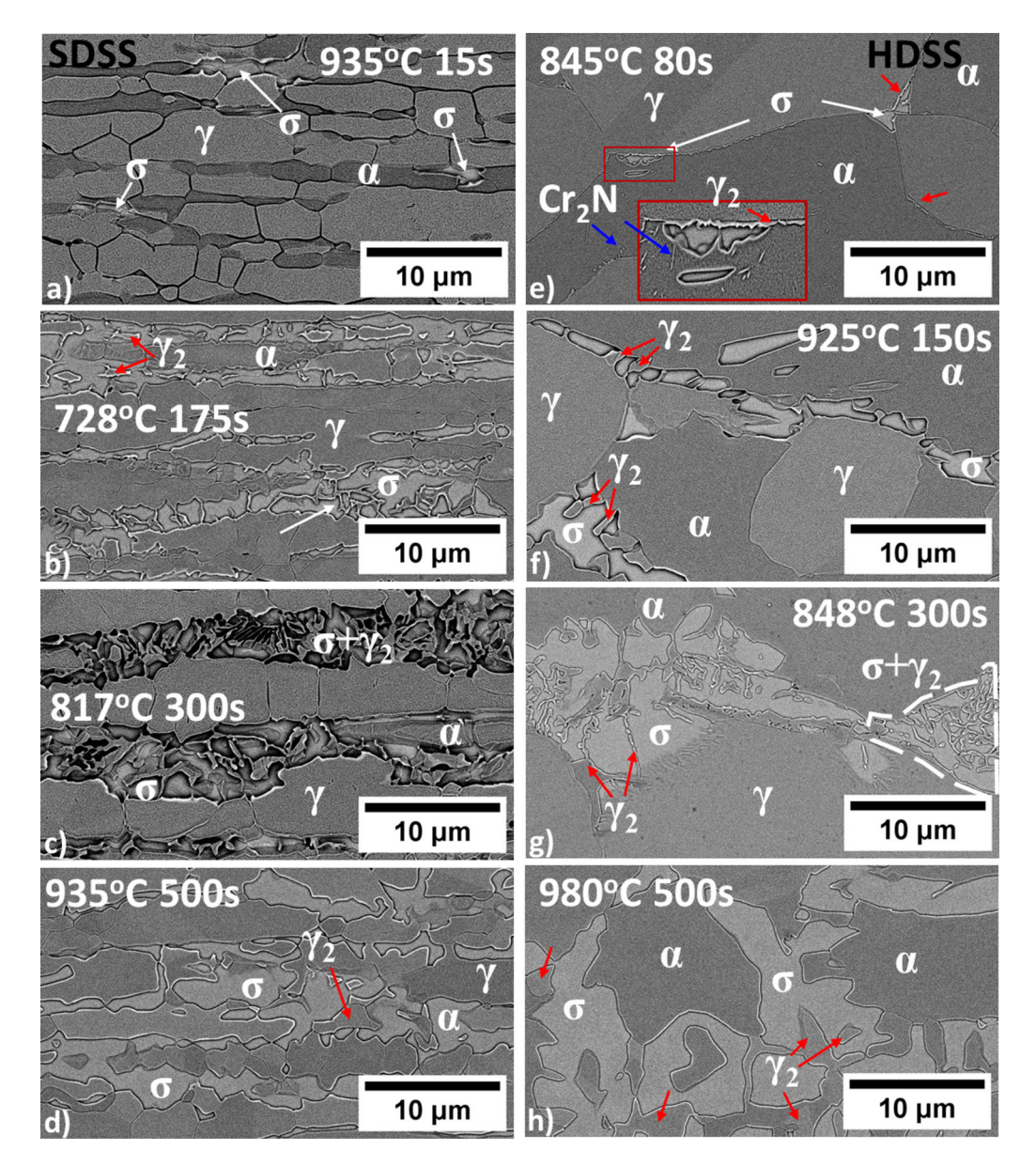


Fig. 6—Sigma phase evolution as a function of heat treatment on the SDSS, left column, (a-d) and HDSS, right column, (e-h) solubilized microstructure. White arrows mark the sigma phase presence, red arrows mark secondary austenite presence, and blue arrows show the chromium nitrides presence.

structure is present in the center of the image, resulting from cellular precipitation following either the Tu and Turnbull's^[55,56] or the Fournelle and Clark's^[57] cell nucleation mechanisms.^[58]

Further sigma phase formation is evident at 500 seconds, Figure 6(d). Due to the higher temperature and longer duration, sigma phase nucleation and growth extend, resulting in a volume fraction of 26.32 ± 1.23 pct. Although fewer nuclei are formed at the high temperature, extensive growth occurs, leading to the formation of large plates of sigma phase and secondary austenite. This separate precipitation phenomenon is referred to as divorced precipitation, as it occurs independently from each other. [59]

Equivalently, the solubilized HDSS Figure 6(e-h) shows a slower sigma phase transformation. The blue

arrows mark the chromium nitride presence. It is known that the sigma phase morphology depends on the transformation temperature. However, this dependence was not only seen as a function of temperatures but also as a function of time. The characteristic sigma/secondary austenite lamellar structure resulting from the eutectoid ferrite decomposition $\alpha \to \sigma + \gamma_2$ is not often seen at heat treatment times up to $100 \text{ s.}^{[45,59,60]}$

Figure 6(e) illustrates the initial stages of sigma phase transformation at 845 °C in 80 s. Precipitation initiates at the α/γ interfaces, particularly at triple corners, accompanied by the formation of secondary austenite extending from the austenite grain. A slim 2.5 μ m² sigma phase grain is observed at an α/γ_2 interface within the red box. Chromium nitride presence is indicated by blue arrows, while red arrows mark the precipitation of

Table IV. SDSS and HDSS JMAK Avrami's Exponent n Calculated from the Experimental Data

	Super Duplex Stainless Steel				Hyper Duplex Stainless Steel				
	1st Slope	2nd Slope	Kinetics Mechanism Transition		1st Slope	2nd Slope	Kinetics M	Kinetics Mechanism Transition	
Temp [°C]	n1	n2	Time [s]	Vol fraction [pct]	n1	n2	Time [s]	Vol fraction [pct]	
725	0.42	0.71	150	1.5	N/A	N/A	N/A	N/A	
750	0.81	1.03	150	3.8	N/A	N/A	N/A	N/A	
775	0.83	0.76	150	5.5	2.598	0.9687	250	3.0	
800	1.10	0.50	150	9.5	2.79	0.806	250	5.4	
825	1.01	0.45	150	12	2.5286	0.6	250	8.0	
850	1.07	0.40	150	13.5	2.764	0.4922	250	10.0	
875	1.44	0.33	60	12	2.1676	0.57	250	11.0	
900	1.38	0.41	60	11	1.924	0.74	250	11.0	
925	1.27	0.62	60	11	1.66	0.856	250	10.1	
950	1.11	0.57	100	10.5	1.74	0.881	250	9.0	
975	1.09	0.42	60	7	2.06	1.125	250	7.1	
1000	0.66	0.63	150	5.1	2.23	1.092	250	4.9	
1025	0.67	0.87	150	2.3	N/A	N/A	N/A	N/A	
Average	0.99	0.59			2.25	0.81	,	,	
Max	1.44	1.03			2.79	1.13			
Min	0.42	0.33			1.66	0.49			

Values are presented for the first slope (discontinuous precipitation or interface-controlled growth), second slope (diffusion-controlled growth), and the respective sigma volumetric fraction at the kinetics mechanism change.

secondary austenite. At this temperature, below the maximum kinetics, a volume fraction of 0.04 ± 0.03 pct of sigma phase is detected.

Close to the maximum kinetics temperature, 4.67 ± 2.40 pct volume of sigma phase forms in 150 seconds at 925 °C, Figure 6(f). Sigma phase plates precipitate, together with larger plates of secondary austenite indicated by red arrows. The precipitate grains grow along α/γ interfaces and within ferrite grains.

At 848 °C, 14.5 \pm 0.84 pct volume of sigma phase is formed, primarily observed in $\sigma + \gamma 2$ lamellar colonies with varying lamella thickness, Figure 6(g). A larger sigma phase colony with large plates is seen on the left side, while a more refined colony is marked by the white-dashed line on the right side. The morphology combines divorced precipitation and cellular precipitation, in which the colony morphology depends on the nucleation process. [58]

Figure 6(h) presents the microstructure formed at 980 °C for 500 seconds. Although the ferrite eutectoid decomposition $\alpha \to \sigma + \gamma 2$ is still present, the lamellar structure is not observed. Divorced precipitation dominates, with significant growth of sigma phase plates and non-uniformly spaced secondary austenite grains.

C. Kinetics Calculations

The Johnson-Mehl-Avrami-Kolmogorov JMAK kinetics approach^[3,25,45,52,62-65] have been successfully describe sigma phase kinetics in DSS.^[3,52,53,62,64,66-69] This research utilizes experimental TTT maps and CALPHAD modeled data for both materials. The phase transformation data is plotted using the linearized JMAK equation to obtain Avrami's exponent (*n*) and the time activation pre-exponent variable (*k*).

Linearized plots are presented at temperatures below, close to, and above the maximum kinetics temperature (775 °C, 900 °C, and 975 °C). Both materials exhibit double kinetics behavior at all temperatures, indicated by strong inflection changes on the plots, suggesting a change in the sigma phase kinetics mechanism. The transformation is divided into two linear stages: the first mechanism (triangular markers) with a steeper n, and the second mechanism (square markers) with a smaller n. This change in Avrami's exponent n corresponds to a shift in kinetics mechanism, also reported in the literature. [3,26,44,52,53]

Elmer et al., [3] Dos Santos et al., [52] and Da Fonseca et al. [25] identify double kinetics as an initial stage of discontinuous precipitation or interface-controlled growth, followed by a second stage of diffusion growth in both duplex and super duplex stainless steels. Marques et al. [53] state that the first kinetic stage is strongly influenced by the chi phase acting as a sigma phase nucleation site, while the second stage involves diffusion growth into the ferrite matrix.

With reference to Christian's^[44] Avrami classification, the calculated n implies that both materials exhibit a primary kinetic mechanism akin to discontinuous precipitation, eutectoid reactions, and interface-controlled growth, while the secondary kinetic mechanism follows diffusion-controlled growth. The shift in kinetics is driven by nucleation site saturation rather than time limitations. Some inflection changes are observed at very short times, but the n and k calculated at these points do not align with experimental phase transformation. However, calculations at inflections with extended times yield closer results to experimental data.

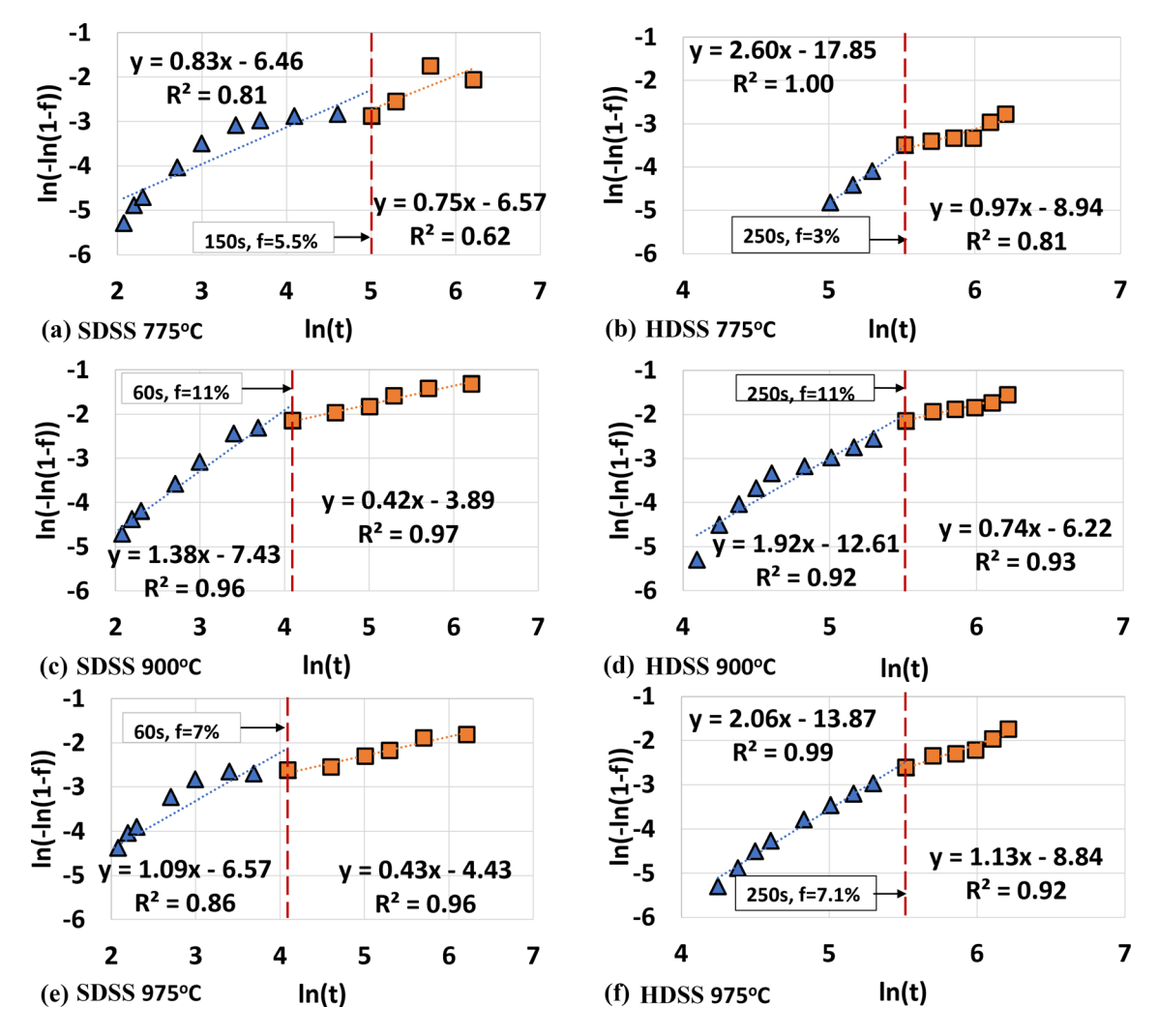


Fig. 7—Solubilized microstructure JMAK linearized plots sigma phase kinetics on SDSS (775 °C (a), 900 °C (c), and 975 °C (e)) and HDSS (775 °C (b), 900 °C (d), and 975 °C (f)). The dominant kinetics mechanism change from kinetic mechanism from discontinuous precipitation and interface-controlled growth to diffusion-controlled growth is seen to occur at distinct times and phase volume fractions for each temperature on the SDSS. Conversely the HDSS resulted on a change of slope at repeatedly at 250 s but with different sigma phase volumes.

At temperatures below the kinetics peak, SDSS demonstrates nearly linear growth of sigma phase volume fraction during the kinetics mechanism transition as temperature varies. The peak, reaching 13.5 pct at 850 °C, precedes a decline, according to Table IV. Transformation times exhibit converse behavior, beginning with longer times, minimizing at the peak kinetics temperature, and then increasing. In contrast, HDSS sigma phase volume formation during kinetics mechanism transition follows a parabolic trend with temperature. In terms of time, this consistently occurs at 250 s or ln(t) = 5.5 (Figure 7). Dos Santos *et al.* [52] previously established that variable kinetics mechanism transition times are temperature dependent.

Christian^[44] further outlines that within discontinuous precipitation and interface-controlled growth (n between 1 and 4), distinct n values might delineate specific formation conditions. Here, n = 1 suggests "grain boundary nucleation after saturation," while n = 2 indicates "grain edge nucleation after saturation."

Table IV displays calculated Avrami's exponent (n) for each temperature in initial and secondary kinetics mechanisms. In the initial kinetics, resembling discontinuous precipitation or interface-controlled growth, SDSS exhibits an n range with an average near 1, indicating grain boundary nucleation after saturation. [44] In contrast, HDSS averages 2.25, suggestive of grain edge nucleation after saturation. [44]

As commonly observed in transformations, n remains somewhat temperature independent while k varies significantly. This research observes substantial n variation across the precipitation temperature range for both materials. Notably, closer to the curve's apex, the maximum kinetics near the curve's apex reveals low-variability Avrami's exponent behavior, irrespective of the dominant kinetics mechanism. Multiple authors assumed the calculated average constant throughout all the temperatures. Occupantly Conversely, k varies multiple orders of magnitude as a function of temperature, and an average value cannot be considered. Therefore, this research used the average Avrami's n exponent and

Table V. Sigma Phase Formation JMAK Kinetics Equations and Calculated Sigma Phase Activation Energies Q_{σ} on Both Materials (SDSS and HDSS) of the Nucleation Mechanism, Growth Mechanism, and Nucleation Mechanism Using CALPHAD Data

	SI	OSS	HDSS		
Kinetics Mechanism	Kinetic Equation	Activation Energy [kJ mol ⁻¹]	Kinetic Equation	Activation Energy [kJ mol ⁻¹]	
Discontinuous precipitation or interface-controlled growth (experimental data)	$f = 1 - e^{(-k_{SD1}t^{0.99})}$	56.4	$f = 1 - e^{(-k_{HD1}t^{2.25})}$	490.0	
	$f = 1 - e^{(-k_{SD2}t^{0.59})}$	309.6	$f = 1 - e^{(-k_{HD2}t^{0.81})}$	247.6	
Discontinuous precipitation or interface-controlled growth (CALPHAD data)	$f = 1 - e^{(-k_{SDc}t^{1.52})}$	666.1	$f = 1 - e^{(-k_{HD2}t^{0.81})}$ $f = 1 - e^{(-k_{SDc}t^{2.23})}$	1500.0	

calculated k at 25 °C increments from the experimental precipitation data. This approach results in a single Avrami-type equation for each slope of the sigma phase transformation, where n is a constant number and k is an array of values as a function of the temperature. Within the precipitation temperature range, at temperatures in between the calculated k values, interpolation can be used to obtain k at a specific temperature.

Indicated by the second slope of diffusion growth, SDSS exhibits Avrami's exponent values of 0.33 to 1.03, whereas HDSS ranges from 0.49 to 1.13. This value spectrum implies needle or plate thickening within the diffusional growth kinetics mechanism. [44] These findings align closely with those of other authors [3,52,53] across different Duplex Stainless Steel families.

Notice that k varies for each kinetic mechanism and temperature. Hence, k_{SDI} corresponds to a matrix of k values based on temperature for SDSS in the first slope. Analogously, there are matrices for the second slope of SDSS, k_{SD2} , as well as for both slopes of HDSS, k_{HD1} and k_{HD2} . Additionally, k_{SDc} and k_{HDc} stand for the JMAK reaction rates in relation to the kinetics calculations' temperature using the CALPHAD data.

By utilizing the equation $k = k_0 e^{(-\frac{V_e}{kT})}$, the activation energy was computed through plotting $ln(k) \times 1/T$ via linear coefficient data regression below the maximum kinetics temperature. The activation energy for the sigma phase is presented in Table V, valid only up to 900 °C due to the region's approximately linear behavior in the plot. Typically, the nucleation activation energy exceeds the growth activation energy, 3,52,64 as seen in HDSS. However, SDSS samples under assessment exhibit relatively low values, indicating favorable nucleation conditions over diffusion. Notably, multiple nuclei are typically observed during rapid transformation times, as also evident in the interpolated experimental TTT map (Figure 4), where sigma is detected at short aging times such as 5 s and 10 s.

In the second slope, representing diffusional growth mechanism, HDSS demonstrates an *n* value and activation energy higher than SDSS, indicating easier growth in the former. Despite this, a volumetric comparison from Figure 4 does not suggest a higher SDSS transformation up to 10 pct. However, it is important to consider that SDSS exhibits a growth activation energy higher than HDSS, while the nucleation activation energy of HDSS is much lower than its counterpart.

As a result, the overall sigma phase formation rate remains higher on SDSS compared to HDSS when SDSS growth is impeded. This outcome is attributed to a combination of factors, including a higher nucleation rate, extensive interface per unit volume leading to increased nucleation density sites, and a greater Cr and Mo content in the ferrite. Both materials demonstrate growth activation energies surpassing the reported Cr-diffusion activation energy in ferrite (250.6 kJ mol⁻¹) and austenite (291.6 kJ mol⁻¹).

D. Kinetics Analytical Calculations from the CALPHAD Model

The JMAK calculation approach holds pivotal significance within the realm of Integrated Computational Materials Engineering (ICME) applications, enabling a concise equation and an array to potentially encapsulate sigma phase formation across varying temperatures. An additional merit of the ICME approach lies in its ability to minimize the requisite experimental precipitation data. This efficiency stems from the CALPHAD model's adeptness in calibration through experimental data, showcasing commendable congruence between modeled and actual data. A strategic integration emerges by envisaging a single JMAK equation derived from the CALPHAD model, thereby facilitating the verification of compositional influences on sigma phase formation. To this end, the JMAK methodology is employed congruently with the previously outlined approach for modeled CALPHAD Time-Temperature-Transformation (TTT) curves encompassing sigma fractions of 1, 3, 5, 7, and 10 pct.

Considering the intrinsic limitations of the CAL-PHAD kinetics model, which predominantly addresses nucleation and initial growth, the ambit of JMAK calculations is confined to sigma phase volumetric fractions below 10 pct. The linearized plots evince commendable linearity on both HDSS and SDSS, as visually depicted in Figure 8. As expected, the noted shift in kinetics mechanism remains absent, which can be ascribed to the anticipatory notion that such a transition occurs at a higher volumetric fraction than the employed dataset's limit of 10 pct. This divergence is plausibly attributed to the depletion of nucleation sites, thus, lending insight into the underlying dynamics of this phenomenon.

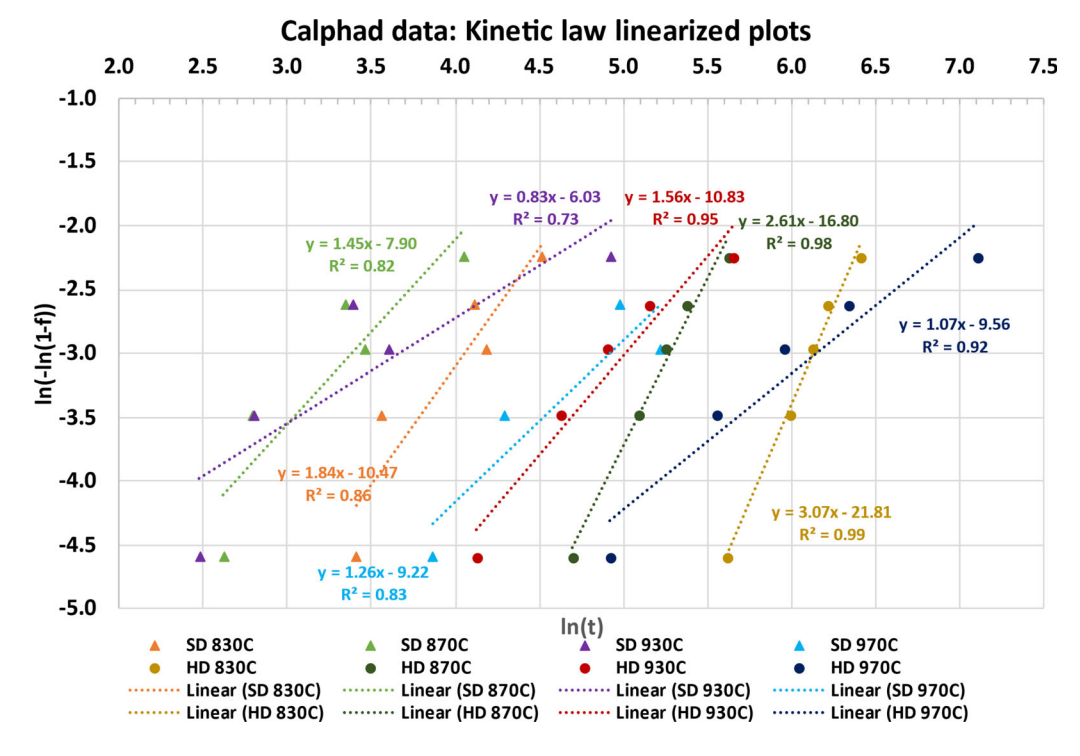


Fig. 8—Kinetic law linearized plot from the CALPHAD-based kinetic data. Linear regressions of transformations at 830 °C, 870 °C, 930 °C, and 970 °C for both materials, SDSS markers in triangles and HDSS markers in circles.

The linearized plots derived from the CALPHAD data reveal an average Avrami's exponent, n, of 1.52 for SDSS and 2.23 for HDSS. These calculated averages closely align with the values obtained from experimental data, which are 0.99 and 2.25 respectively (Table IV). However, disparities emerge in the activation energies associated with the JMAK calculations from CALPHAD data, differing from those yielded by the JMAK experimental approach. This divergence arises from the inherent temperature dependence of both JMAK parameters, n and k. While notable, the contrast in kinetics between the experimental data, the experimentally derived JMAK kinetics, and the CALPHAD-based JMAK kinetics remains within reasonable bounds.

In Figure 9, a materials comparison is presented, illustrating the overlap of TTT calculations with experimental data. In addition, the image showcases JMAK calculations based on experimental data for SDSS (a) and HDSS (b), along with JMAK calculations derived from the CALPHAD model data for SDSS (c) and HDSS (d). This comprehensive depiction encapsulates the interplay between empirical and modeled kinetics, providing a visual framework for the observed variations.

Figures 9(a) and (b) reveals that the experimental-based JMAK calculations exhibit satisfactory agreement for the 1 pct sigma phase in both materials. However, noticeable temporal disparities emerge in the 5 and 10 pct curves calculations, particularly evident in the SDSS case (a). The predictions tend to underestimate sigma formation in the SDSS, while the same approach leans towards overestimation in HDSS. This trend is thought to be linked to k calculations, which heavily rely on temperature and the critical activation

energy value (Table V). Ray^[43] highlighted several implications of activation energy in reaction rates: higher activation energies induce greater temperature sensitivity in reactions, while lower values result in reduced temperature dependency. Moreover, such temperature effects become more pronounced at lower temperatures.

The JMAK kinetics employing CALPHAD data align well with CALPHAD model outcomes. Despite the HDSS linearized plots showing a more robust regression fit (see Figure 8) and the CALPHAD n average value closely matching experimental findings, on the SDSS results, Figure 9(c) exhibits excellent outcomes for sigma phase volumetric fractions of 1 and 5 pct. However, a converse situation arises for HDSS, where JMAK kinetics derived from CALPHAD data tend to overpredict sigma phase formation by an order of magnitude.

Nonetheless, it's worth noting that the kinetics calculations based on model data exhibit no significant deviations from the original data. Furthermore, irrespective of material, CALPHAD-based JMAK kinetics calculations consistently lean towards overpredicting sigma phase formation. While this trend may appear cautious, it is inherently safer than the potential consequences of underestimating a potentially detrimental phase transition.

IV. CONCLUSIONS

The kinetics of sigma phase formation in SDSS and HDSS filler metals were evaluated and compared using experimental precipitation data and JMAK analytical

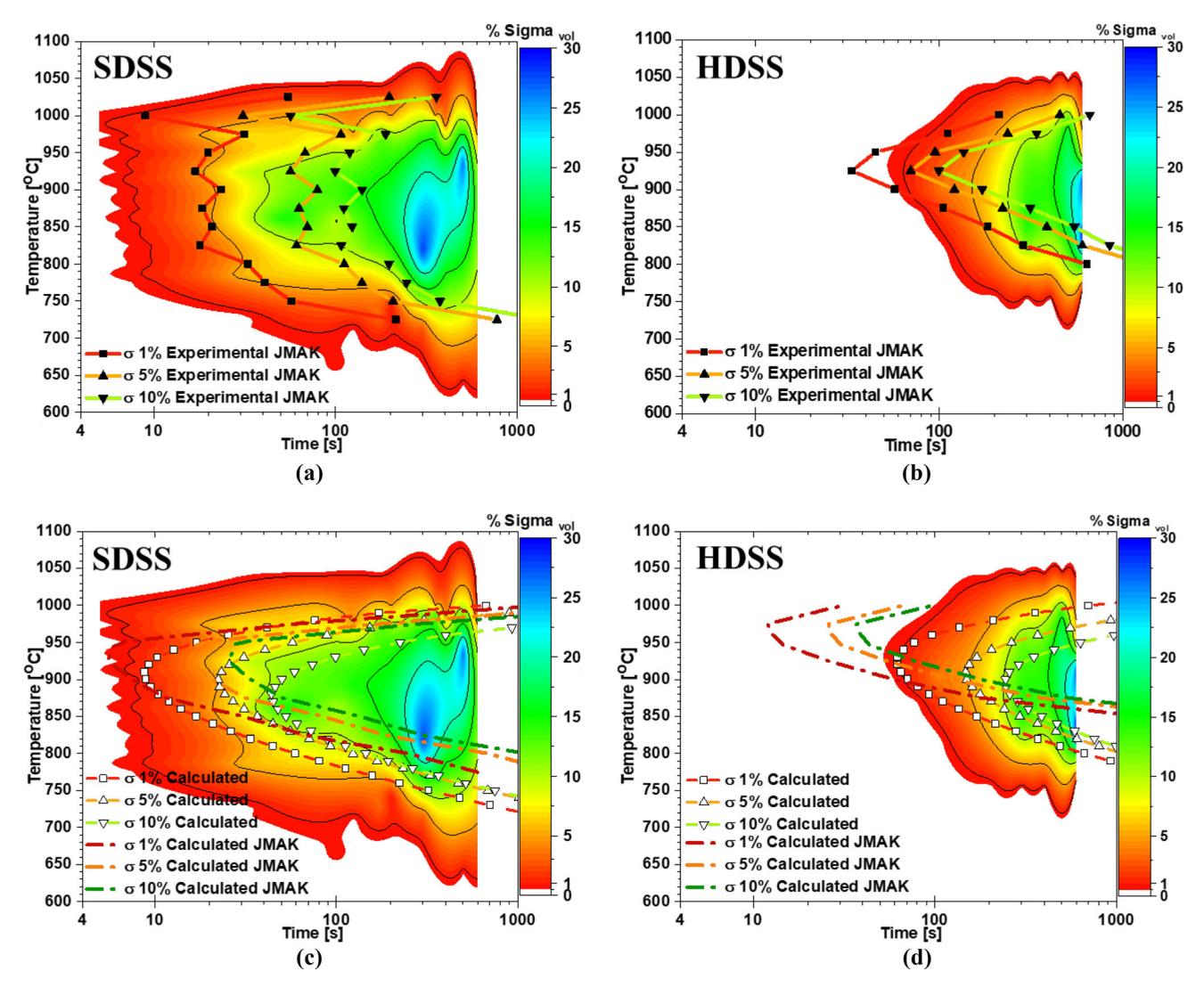


Fig. 9—Calculated JMAK Kinetics. Experimental-based JMAK TTTs overlapped on the experimental kinetics map of (a) SDSS and (b) HDSS. CALPHAD-based JMAK in the dash-dot lines overlapped with the CALPHAD TTT as symbol lines and the experimental kinetic MAP of (c) SDSS and (d) HDSS.

calculations based on both experimental precipitation TTT data and CALPHAD-based calculated TTTs. These kinetics models facilitated a comprehensive understanding of the susceptibility to sigma phase formation in HDSS wire and offered insights in comparison to the widely used SDSS wire. Our findings are summarized as follows:

- 1. In the solubilized condition, SDSS exhibits higher sigma phase kinetics than HDSS. Particularly on the nucleation-governed stage, evident in quicker sigma phase precipitation at shorter treatment times and over a broader temperature range compared to HDSS.
- 2. The SDSS higher sigma phase kinetics is primarily attributed to higher nucleation sites, confirmed through the interface length per volume unit measurements, 374 pct higher than the HDSS in the solubilized condition.
- 3. Besides the higher nucleation sites in the SDSS, the less Cr-rich SDSS presented a ferrite phase richer in Cr. The higher N content of HDSS affects the Cr and Mo partition between phases and phase diffusivity. As a result, the HDSS Cr and Mo are more evenly distributed in both phases, causing austenite enriched in Cr and Mo at the expense of the ferrite content. The HDSS ferrite is about 1 wt pct leaner in Cr than the SDSS ferrite.
- 4. The pivotal role of physical simulation experimental data becomes apparent in its essential contribution to refining computational and analytical models. The highest agreement was at maximum kinetics, TTT curve nose, whereas the borders high and low temperature were compromised, presenting less agreement.
- The JMAK kinetic modeling of sigma phase in both SDSS and HDSS filler metals reveals a dual-stage mechanism. Encompassing an initial

nucleation-controlled and discontinuous precipitation mechanism, succeeded by a diffusion-controlled growth mechanism. The first kinetic mechanism presented Avrami's exponent n indicating grain boundary nucleation after saturation on the SDSS, while the calculated HDSS n exponent indicated grain edge nucleation after saturation. Both materials presented the secondary kinetic mechanism as diffusion-controlled growth, with the SDSS presenting the thickening of plates and the HDSS indicating the thickening of needles.

- 6. The sigma morphologies were compatible with ferrite decomposition ($\alpha \to \sigma + \gamma_2$), presenting sigma and secondary austenite. However, the discontinuous "lamellar" morphology was predominantly observed at temperatures below the maximum kinetics and in the diffusion-controlled stage.
- 7. Experimental data are critical to adjust and validate the kinetics model. JMAK calculations were effective on the experimental data. Even when using experimental-adjusted CALPHAD-based TTT curves, the JMAK calculations did not matched the experimental data.

ACKNOWLEDGMENTS

The authors thank the Manufacturing and Materials Joining Innovation Center (Ma2JIC) and NSF (IUCRC program, awards 1539992, 1822144, and 2052747). OSU Center for Electron Microscopy and Analysis (CEMAS) for its supporting microscopy. Industry mentors R. Menon, M. Denault, P.Björnstedt, and V. Hosseini for providing the material and fruitful technical discussions. N. Daubenmier for the support for Python coding, and Dr. Eric Brizes for the support and reference on the kinetics approach.

DATA AVAILABILITY

The raw/processed data required to reproduce these findings cannot be shared at this time as the data also forms part of an ongoing study.

COMPETING INTEREST

The authors declare the following financial interests/personal relationships which may be considered as potential competing interests: Andres Acuna reports financial support was provided by Manufacturing and Materials Joining Innovation Center.

DECLARATION OF GENERATIVE AI AND AI-ASSISTED TECHNOLOGIES IN THE WRITING PROCESS

During the preparation of this work the author(s) used ChatGPT 3.5 and Grammarly in order to readproof, enhance grammar, and reading flow. After using this tool/service, the author(s) reviewed and edited the content as needed and take(s) full responsibility for the content of the publication.

SUPPLEMENTARY INFORMATION

The online version contains supplementary material available at https://doi.org/10.1007/s11661-024-07442-4.

NOMENCLATURE

Time_Temperature_Transformation

TTT

111	Time-Temperature-Transformation
JMAK	Johnson-Mehl-Avrami-Kolmogorov
PREn	Pitting Resistance Equivalent Number
DSS	Duplex Stainless Steel
SDSS	Super Duplex Stainless Steel
	(40 < PREn > 45)
HDSS	Hyper Duplex Stainless Steel (PREn > 48)
α	Ferrite phase
γ	Austenite phase
$\gamma 2$	Secondary austenite phase
σ	Sigma phase
LOM	Light Optical Microscopy
SEM	Scanning Electron Microscopy
EBSD	Electron Backscattered Diffraction
BSE	Backscattered Electrons
TCFE11	CALPHAD Thermodynamic Database
MOBFE6	CALPHAD Mobility Database

OPEN ACCESS

This article is licensed under a Creative Commons Attribution 4.0 International License, which permits use, sharing, adaptation, distribution and reproduction in any medium or format, as long as you give appropriate credit to the original author(s) and the source, provide a link to the Creative Commons licence, and indicate if changes were made. The images or other third party material in this article are included in the article's Creative Commons licence, unless indicated otherwise in a credit line to the material. If material is not included in the article's Creative Commons licence and your intended use is not permitted by statutory regulation or exceeds the permitted use, you will need to obtain permission directly from the copyright holder. To view a copy of this licence, visit http://creat ivecommons.org/licenses/by/4.0/.

REFERENCES

- M. Knyazeva and M. Pohl: Metallogr. Microstruct. Anal., 2013, vol. 2, pp. 113–21. https://doi.org/10.1007/s13632-013-0066-8.
- API RP 582 Welding Guidelines for the Chemical, Oil, and Gas Industries, A. P. I. API, 1220 L Street, NW, Washington, DC, 2016.

- J.W. Elmer, T.A. Palmer, and E.D. Specht: *Metall. Mater. Trans.* A, 2007, vol. 38A, pp. 464–75. https://doi.org/10.1007/s11661-006-9076-3
- J.O. Nilsson: Mater. Sci. Technol., 1992, vol. 8, pp. 685–700. h ttps://doi.org/10.1179/mst.1992.8.8.685.
- E.O. Hall and S.H. Algie: SIGMA PHASE. J. Inst. Met., 1966, vol. 94, pp. 61.
- J.O. Nilsson, P. Kangas, T. Karlsson, and A. Wilson: *Metall. Mater. Trans. A*, 2000, vol. 31A, pp. 35–45. https://doi.org/10.1007/s11661-000-0050-1.
- 7. C.-C. Hsieh: ISRN Metall., 2012, vol. 2012, pp. 1-6.
- S.K. Bonagani, K. Chandra, K.V. Ravikanth, H. Donthula, S. Roychowdhury, and V. Kain: *Mater. Sci. Eng. A*, 2023, https://doi.org/10.1016/j.msea.2023.145763.
- V.I. Kopylov, et al.: Metals, 2023, https://doi.org/10.3390/me t13010045.
- H.H. Lu, X.Q. Shen, and W. Liang: Acta Metall. Sin., 2021, vol. 34, pp. 1285–95. https://doi.org/10.1007/s40195-021-01227-z.
- 11. H.H. Lu, H.K. Guo, and W. Liang: *Mater Charact*, 2022, https://doi.org/10.1016/j.matchar.2022.112050.
- C.P. Lu, X.S. Shen, X.J. Cheng, C.W. Du, and H.C. Ma: J. Mater. Eng. Perform., 2023, https://doi.org/10.1007/s11665-023-08949-4.
- Z.Q. Zhang, H.Y. Jing, L.Y. Xu, Y.D. Han, and L. Zhao: Investigation on microstructure evolution and properties of duplex stainless steel joint multi-pass welded by using different methods. *Mater. Des.*, 2016, vol. 109, pp. 670–85. https://doi.org/10.1016/j. matdes.2016.07.110.
- Y.X. Han, R.T. Chi, Q.C. Chen, B. Wang, W. Liu, and Y.L. He: *J. Mater. Res. Technol.*, 2023, vol. 26, pp. 2560–74. https://doi.org/10.1016/j.jmrt.2023.08.034.
- Y. Han, et al.: Tungsten, 2023, vol. 5, pp. 419–39. https://doi.org/ 10.1007/s42864-022-00168-z.
- L.K.D. Inácio, W. Wolf, B.C.B. de Leucas, G.C. Stumpf, and D.B. Santos: *Mater Charact*, 2021, https://doi.org/10.1016/j.matc har.2020.110802.
- T.R. Dandekar, R.K. Khatirkar, D. Mahadule, J. Chavhan, and D. Kumar: *Mater. Today Commun.*, 2022, https://doi.org/10.1016/j.mtcomm.2022.104913.
- I.J. Marques, F.J. Silva, and T.F.A. Santos: *J. Alloys Compd.*, 2020, https://doi.org/10.1016/j.jallcom.2019.153170.
- M.T.G. de Sampaio, et al.: J. Mater. Res. Technol., 2023, vol. 26, pp. 8149–64. https://doi.org/10.1016/j.jmrt.2023.09.106.
- Z.X. Liu, Y. Xie, L.X. Zhang, W.Z. Zhao, C.Z. Zhao, and H. He: *Mater. Today Commun.*, 2023, https://doi.org/10.1016/j.mtcomm. 2023.106215.
- A.K. Maurya, C. Pandey, and R. Chhibber: Int. J. Pressure Vessels Piping, 2021, https://doi.org/10.1016/j.ijpvp.2021.104439.
- E.M. Cojocaru, D. Raducanu, A. Nocivin, and V.D. Cojocaru: Adv. Res., 2021, vol. 30, pp. 53–61. https://doi.org/10.1016/j.jare. 2020.11.005.
- 23. A.G.C. dos Santos, et al.: *J. Mater. Res. Technol*, 2021, vol. 15, pp. 2625–32. https://doi.org/10.1016/j.jmrt.2021.09.051.
- A.S. Fedorov, A.I. Zhitenev, D.A. Strekalovskaya, A.A. Kur, and A.A. Alkhimenko: *Metals*, 2021, https://doi.org/10.3390/met111111750.
- G.S. da Fonseca, P.S.N. Mendes, and A.C.M. Silva: *Metals*, 2019, https://doi.org/10.3390/met9010034.
- G.S. da Fonseca, P.M. de Oliveira, M.G. Diniz, D.V. Bubnoff, and J.A. de Castro: *Mater. Res. Ibero Am J. Mater.*, 2017, vol. 20, pp. 249–55. https://doi.org/10.1590/1980-5373-mr-2016-0436.
- L. O. P. da Silva, T. N. Lima, F. M. dos Santo, Jr., B. Callegari, L. F. Folle, and R. S. Coelho, *Crystals*, vol. 14, no. 3, 204, 2024. h ttps://doi.org/10.3390/cryst14030204.
- B.B. Zhang, Z.H. Jiang, H.B. Li, S.C. Zhang, H. Feng, and H. Li: Mater Charact, 2017, vol. 129, pp. 31–39. https://doi.org/10.1016/j.matchar.2017.04.018.
- D.H. Kim, N.H. Kim, and H.W. Lee: *Mater. Sci. Technol.*, 2020, vol. 36, pp. 783–92. https://doi.org/10.1080/02670836.2020. 1743575.

- B.B. Zhang, et al.: Mater Charact, 2021, https://doi.org/10.1016/j. matchar.2021.111096.
- J. Wang, W.L. Chen, H.J. Meng, Y.S. Cui, C.L. Zhang, and P.D. Han: *J. Iron. Steel Res. Int.*, 2019, vol. 26, pp. 452–61. https://doi.org/10.1007/s42243-018-0175-3.
- 32. A. Acuna, A. Ramirez, R. Menon, P.-Å. Björnstedt, and L. Carvalho, in *ASME 2021 Pressure Vessels & Piping Conference*, 2021, vol. 4, V004T06A042. https://doi.org/10.1115/PVP2021-62042.
- 33. A. Acuna and A.J. Ramirez: *Mater Charact*, 2023, vol. 200, p. 112832. https://doi.org/10.1016/j.matchar.2023.112832.
- A. Acuna, A. Ramirez, and K.C. Riffel: Sci. Technol. Weld. Join., 2023, https://doi.org/10.1080/13621718.2023.2246719.
- A. Acuna, K.C. Riffel, and A. Ramirez: Mater Charact, 2023, h ttps://doi.org/10.1016/j.matchar.2023.113433.
- 36. G. Chai and P. Kangas, Super and hyper duplex stainless steels: structures, properties and applications. *21st European Conference on Fracture*, (*Ecf21*), vol. 2, pp. 1755–62, 2016. https://doi.org/10.1016/j.prostr.2016.06.221.
- M.L. Stein: Interpolation of spatial data: some theory for kriging, Springer, Berlin, 1999.
- 38. A.J. Ramirez, J.C. Lippold, and S.D. Brandi: *Metall. Mater. Trans. A*, 2003, vol. 34A, pp. 1575–97. https://doi.org/10.1007/s11661-003-0304-9.
- A. Acuna, A. Ramirez, and K.C. Riffel: Sci. Technol. Weld. Join., 2023, vol. 28, pp. 885–93. https://doi.org/10.1080/13621718.2023. 2246719
- 40. W.A. Johnson and R.F. Mehl: *Trans. Am. Inst. Min. Metall. Eng.*, 1939, vol. 135, pp. 416–42.
- M. Avrami: J. Chem. Phys., 1939, vol. 7, pp. 1103–12. https://doi. org/10.1063/1.1750380.
- 42. M. Avrami: *J. Chem. Phys.*, 1941, vol. 9, pp. 177–84. https://doi.org/10.1063/1.1750872.
- 43. H.S. Ray and S. Ray: *Kinetics of metallurgical processes*, Springer, Berlin, 2018.
- 44. J.W. Christian: *The theory of transformations in metals and alloys*, 3rd ed. Pergamon, Amsterdam, 2002, p. 2.
- 45. B. Josefsson, J.-O. Nillson, and A. Wilson, Phase transformations in duplex steels and the relation between continuous cooling and isothermal heat treatment, presented at the Duplex Stainless Steels '91, France, 1991.
- 46. S. Hertzman, W. Roberts, and M. Lindenmo, Microstructure and Properties of Nitrogen Alloyed Duplex Stainless Steel After Welding Treatments, presented at the Duplex Stainless Steel '86, The Netherlands, 1986.
- 47. S. Bernhardsson, The Corrosion Resistance of Duplex Stainless Steels, presented at the Duplex Stainless Steels '91, France, 1991.
- 48. Y. Yang, B. Yan, J. Li, and J. Wang: *Corros. Sci.*, 2011, vol. 53, pp. 3756–63. https://doi.org/10.1016/j.corsci.2011.07.022.
- K.C. Russell: Adv. Coll. Interface. Sci., 1980, vol. 13, pp. 205–318. https://doi.org/10.1016/0001-8686(80)80003-0.
- 50. R. Wagner, R. Kampmann, and P. W. Voorhees, in *Phase Transformations in Materials*, 2001, pp. 309–407.
- 51. R. Kampmann and R. Wagner, Kinetics of precipitation in metastable binary alloys theory and application to Cu-1.9 at pct Ti and Ni-14 at pct Al, First edition. ed. (Acta-scripta metallurgica proceedings series, no. 2). Oxford Oxfordshire; New York: Pergamon Press, 1984, pp. 91-103.
- 52. D.C. Dos Santos and R. Magnabosco: *Metall. Mater. Trans. A*, 2016, vol. 47A, pp. 1554–65. https://doi.org/10.1007/s11661-016-3323-7
- I.J. Marques, A.D.A. Vicente, J.A.S. Tenorio, and T.F.D. Santos: *Mater. Res. Ibero Am. J. Mater.*, 2017, vol. 20, pp. 152–58. h ttps://doi.org/10.1590/1980-5373-mr-2016-1060.
- 54. M. Pohl and O. Storz: *Int. J. Mater. Res.*, 2004, vol. 95, pp. 631–38.
- K.N. Tu and D. Turnbull: Acta Metall., 1967, vol. 15, pp. 1317–2000. https://doi.org/10.1016/0001-6160(67)90007-7.
- K.N. Tu and D. Turnbull: Acta Metall., 1967, vol. 15, p. 369. h ttps://doi.org/10.1016/0001-6160(67)90214-3.

- 57. R.A. Fournelle and J.B. Clark: *Metall. Trans.*, 1972, vol. 3, pp. 2757–67. https://doi.org/10.1007/BF02652842.
- 58. D. Duly and Y. Brechet: *Acta Metall. Mater.*, 1994, vol. 42, pp. 3035–43. https://doi.org/10.1016/0956-7151(94)90400-6.
- 59. I. Machado: Transformações de fase no estado sólido em alguns aços inoxidáveis austeníticos e ferríticos-austeníticos (dúplex) contendo altos fatores de nitrogênio, Universidade de São Paulo, São Paulo, Escola Politécnica, 1999.
- 60. M. Pohl and O. Storz: *Zeitsch. Metall.*, 2004, vol. 95, pp. 631–38. h ttps://doi.org/10.3139/146.017999.
- A.J. Ramirez, S.D. Brandi, and J.C. Lippold: Sci. Technol. Weld. Join., 2004, vol. 9, pp. 301–13. https://doi.org/10.1179/ 136217104225021715.
- 62. P. Ferro, F. Bonollo, and G. Timelli: *Metall. Ital.*, 2012, vol. 5, pp. 7–12
- S.M. Kim, J.S. Kim, K.T. Kim, K.-T. Park, and C.S. Lee: *Mater. Sci. Eng. A*, 2013, vol. 573, pp. 27–36. https://doi.org/10.1016/j.msea.2013.02.044.
- 64. R. Magnabosco: *Mater. Res. Ibero Am J. Mater.*, 2009, vol. 12, pp. 321–27. https://doi.org/10.1590/s1516-1439200900300012.

- A. Wilson and J.O. Nilsson: Scand. J. Metall., 1996, vol. 25, pp. 178–85
- 66. T. A. Palmer, J. W. Elmer, J. Wong, S. S. Babu, and J. M. Vitek, *Investigation of the kinetics of the ferrite/austenite phase transformation in the HAZ of a 2205 duplex stainless steel weldment* (Trends in Welding Research, Proceedings). 2003, pp. 23–28.
- 67. P. Ferro, A. Fabrizi, and F. Bonollo: *Acta Metall. Sin.*, 2016, vol. 29, pp. 859–68. https://doi.org/10.1007/s40195-016-0462-6.
- 68. P. Ferro, F. Bonollo, A. Fabrizi, G. Timelli, and G. Mazzacavallo: *Metall. Ital.*, 2013, vol. 5, pp. 25–29.
- 69. P. Ferro and F. Bonollo: *Metall. Mater. Trans. A*, 2012, vol. 43, pp. 1109–16. https://doi.org/10.1007/s11661-011-0966-7.
- A.W. Bowen and G.M. Leak: *Metall. Trans.*, 1970, vol. 1, p. 1695. https://doi.org/10.1007/bf02642019.

Publisher's Note Springer Nature remains neutral with regard to jurisdictional claims in published maps and institutional affiliations.